The 2006 Eruption of Augustine Volcano, Alaska
Power, J.A., Coombs, M.L., and Freymueller, J T., editors
U.S. Geological Survey Professional Paper 1769

Chapter 23

The 2006 Eruption of Augustine Volcano—Combined Analyses of Thermal Satellite Data and Reduced Displacement

By Saskia M. van Manen[1], Jonathan Dehn[2], Michael E. West[2], Stephen Blake[1] and David A. Rothery[1]

Abstract

Augustine Volcano erupted explosively after 20 years of quiescence on January 11, 2006, followed by approximately 2 months of dome building and lava extrusion. This is the best monitored eruption in Alaska to date; the diverse complementary datasets gathered enable an interdisciplinary interpretation of volcanic activity. An analysis of reduced displacement (continuous measure of seismic tremor amplitude) and thermal energy output (from satellite imagery) observed between January 1 and April 30, 2006, shows relationships linked to the type of eruptive activity. Three different types of volcanic behavior can be identified as they show specific patterns in the combined data sets: (1) explosive activity, (2) lava extrusion (dome growth), and (3) cooling of erupted products. Explosive activity was characterized by high reduced displacement values but relatively low radiative thermal flux. Lava extrusion occurred in three distinct sequences characterized by increased values of reduced displacement and increased thermal emissions. Two periods of elevated thermal energy output and reduced displacement coincided with times of deflation, suggesting an increase in extrusion rate. Periods of cooling were marked by decreasing thermal emissions and reduced displacement. This work highlights the value of combined observations, which reveal more about the status of an active volcano than individual methods alone.

[1]Volcano Dynamics Group, Department of Earth and Environmental Sciences,The Open University, Walton Hall, Milton Keynes, MK7 6AA U.K.

[2]Alaska Volcano Observatory, Geophysical Institute, University of Alaska Fairbanks, 903 Koyukuk Drive, P.O. Box 757320, Fairbanks, AK 99775-7320.

Introduction

Nearly 20 years after its last eruption, Augustine Volcano (59.361ºN, 153.426ºW; fig. 1) began to erupt on January 11, 2006 (Power and others, 2006). Augustine is an 8 by 11 km volcanic island located in the southern Cook Inlet, approximately 290 km southwest of Anchorage, Alaska. It has erupted 8 times since it was named in 1778 by Captain Cook (Miller and others, 1998). Its summit consists of an andesitic lava dome and lava flow complex, which has repeatedly collapsed resulting in debris avalanches, occasionally triggering tsunamis (Siebert and others, 1995). Currently, the primary hazard from Augustine arises from ash-rich plumes that traverse north Pacific air traffic routes (Miller and Casadevall, 1998). However, hazards also exist for nearby residents in the form of ashfall and tsunamis. An example of this is the 1883 eruption, which caused a tsunami that inundated large sections of Cook Inlet (Siebert and others, 1995; Waythomas and others, 2006).

The 2006 eruption was preceded by seismic unrest that started on April 30, 2005 (Jacobs and McNutt, this volume; Power and Lalla, this volume) and inflation of the edifice that started in July 2005 (Cervelli and others, this volume). Phreatic eruptions were reported throughout December 2005. In the 10 days preceding the first explosive event only three thermal anomalies were found by visual inspection in satellite data. However, more detailed changes in the thermal state of Augustine were observed in the higher resolution thermal camera (Forward Looking Infrared Radiometer, FLIR) data (Wessels and others, this volume). Explosive activity producing ash-rich plumes reaching up to 14 km above sea level (Petersen and others, 2006) started on January 11 and continued intermittently until January 28. Lava extrusion is thought to have commenced around January 13, as indicated by the presence of juvenile glass shards in ash samples (Wallace and

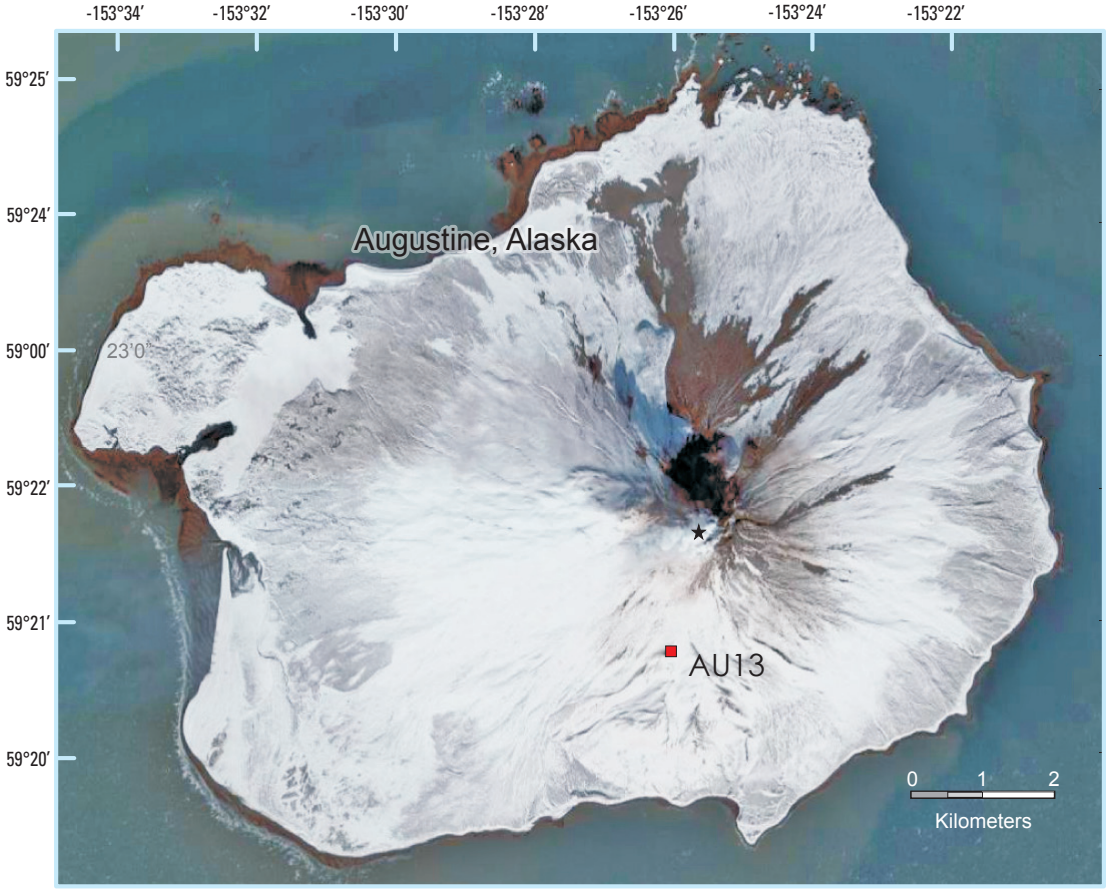

Figure 1. Location figure of Augustine Volcano. This Google Earth™ (DigitalGlobe) image of Augustine Volcano was taken after the 2006 eruption. The snow in the image highlights the location of the newly formed block and ash flows and pyroclastic deposits (all in black) on the north and northeastern slopes. Figure shows location of seismic station AU13, located 1.8 km from the summit of Augustine. This station is the source of the reduced displacement data.

others, this volume). Lava effusion continued until late March, resulting in a lava dome and two short (<1 km) blocky lava flows (Power and others, 2006). The exact date when lava effusion ceased is undocumented by field observations. During the course of the eruption Augustine went through three phases of inflation and two phases of deflation (Cervelli and others, this volume). In addition, numerous rock falls, pyroclastic flows, and block and ash flows were observed, likely related to the growth of the lava dome and flows (Coombs and others, this volume).

Lava dome emplacement is a nonlinear dynamic process accompanied by a wide range of phenomena, including the opening of fissures, increased fumarolic activity, extrusion of lava, earthquakes, dome collapse, explosions, and pyroclastic flows. In addition, phases of quiescence and violence often alternate depending on factors such as extrusion rate, magma rheology and thickness of the cooling top layer (Fink and Griffiths, 1998). Understanding the dynamics involved in the emplacement of lava domes is important because instability can result in collapses accompanied by pyroclastic flows, ash plumes and co-ignimbrite plumes that are capable of reaching air-traffic routes (Woods and Kienle, 1994; Miller and Casadevall, 1998).

This paper presents an interpretation of satellite and reduced displacement data obtained at Augustine Volcano between January 1 and April 30, 2006, spanning the entire eruption and part of the precursory phase, in order to form a more comprehensive understanding of how these signals relate to the observed volcanic activity. Relating thermal signatures to ground activity enhances remote-sensing and seismic monitoring capabilities, particularly in the Alaska-Aleutian-Kamchatka region where satellite data are often the only data source available.

Background

Satellite monitoring provides a means to characterize the thermal states of active volcanoes. Studying satellite-derived data in conjunction with ground-based data and visual observations may help to better understand the nature and significance of the thermal signals. This “ground truthing” permits improved interpretations of the satellite data, making it possible to better gauge volcanic activity at volcanoes monitored solely by remote sensing. Remote sensing of active volcanoes allows near real-time observation of a whole volcano in different parts of the electromagnetic spectrum (Mouginis-Mark and others, 2000). The temporal coverage depends on the satellite used. This study focuses on measurements of thermal flux and total radiated energy, other areas of remote sensing are discussed in other chapters in this volume (Webley and others, this volume; Lee and others, this volume).

This study uses Advanced Very High Resolution Radiometer (AVHRR) data. AVHRR is the primary instrument on the polar orbiting weather satellites operated by the National Oceanographic and Atmospheric Administration (NOAA). Each day, between 10 and 30 AVHRR images with a nadir pixel-size of 1.1 km, in five bands spanning the visible to the infrared, are acquired over the Augustine region. Not all of these images are of suitable quality for study; for example, images with a zenith angle greater than 55° are discarded, as data obtained from them is too geometrically distorted (Harris and others, 1997). The zenith angle is the angle between the local zenith and the line of sight to the satellite. This reduces the number of functional images to approximately half of those obtained. Drawbacks of AVHRR data include its coarse spatial resolution; however, this disadvantage is far outweighed by its high temporal coverage of the Alaska-Aleutian-Kamchatka area because of the polar convergence of the satellite orbits.

Seismology has long been a mainstay of volcano monitoring, as it provides one of the best means of assessing a volcano's state of activity. The central goal of volcano seismology is to understand the subsurface structure of volcanoes and track the movements of fluids, including gas and magma, through this structure. McNutt (2005) notes four main types of seismic signal that are observed at active volcanoes: (1) high-frequency events, also known as volcano-tectonic events (VT), (2) low-frequency events, also termed long-period (LP) events, (3) explosions and (4) volcanic tremor. These events can be divided into two groups based on the origin of their source energies: (1) those where fluid plays an active role in the source mechanism (Aki and others, 1977; Aki and Koyanagi, 1981) and (2) those where magmatic processes provide energy for rock failure (Shaw, 1980; Aki and Koyanagi, 1981; Weaver and others, 1981). The first group involves LP events and volcanic tremor, whereas the second category consists of VT earthquakes. Mixtures of the two types also occur, these are termed hybrid events (Shaw, 1980; Lahr and others, 1994).

Volcanic tremor is a common but poorly understood type of seismic signal that has been documented at more than 160 volcanoes (McNutt, 1994). Difficulty arises from the wide ranging definition of tremor, which covers many different types of behavior. A variety of source models have been proposed, including that it is a sustained sequence of LP events (Latter, 1979; Fehler, 1983; Malone and others, 1983). Others argue for a more continuous source formed by resonance in the conduit, possibly in conjunction with changing physical properties (Neuberg and O'Gorman, 2002; Benoit and others, 2003). Though the exact source of the tremor is debated and likely nonunique, all models associate tremor with the movement of fluids through the volcanic subsurface. Tremor often precedes and accompanies volcanic eruptions, although not all volcanic tremor culminates in eruptions (Julian, 1994).

Reduced displacement (D_r) is a continuous measure of tremor amplitude (Aki and Koyanagi, 1981). Tremor is a sustained phenomenon, because of this it dominates the seismic record when present. Reduced displacement is comparable to the RSAM (Real-time Seismic-Amplitude Measurement) method of Endo and Murray (1991), but it differs in that it adjusts the amplitude for a presumed source. Although this introduces a possible bias to the data, in practice it permits multiple seismic stations to be used together and allows comparisons between different eruptions on a common scale.

McNutt (1994) determined an empirical correlation between tremor amplitude and column height based on the analysis of 21 eruptions at 14 volcanoes. During the 1996 Pavlof (Alaska) eruption, a general relationship between plume height and tremor amplitude was observed by Roach and others (2001). In addition, the size of the observed thermal anomaly steadily increased before the eruption of the largest plumes, which reached an altitude of 10 km above sea level (Roach and others, 2001). However, Nye and others (2002) found that during the 1999 Shishaldin (Alaska) eruption there was a remarkable lack of correlation between reduced displacement and plume height. They also found that thermal anomalies often preceded volcanic tremor associated with strombolian outbursts. Galindo and Dominguez (2002) found good correlations between thermal and seismic data at Colima (Mexico) during 1997–2000. Using AVHRR and seismic data during precursory, effusive, and explosive stages of the eruption they recorded five seismic swarms, four of which coincided with periods of increased summit temperature and strong ash emissions. It is noteworthy that ash emissions were observed prior to the seismic swarms.

Data Acquisition

Thermal Imagery

Between January 1 and April 30, 2006, thermal anomalies centered over Augustine were identified in band 3 (3.55–3.93 μm) in 323 AVHRR images by the automated Okmok II algorithm. Thermally anomalous pixels are those that rise 5°C or more above the mean temperature of the surrounding eight pixels (AVO Remote Sensing Team, 2000). Okmok II improves upon its predecessor, Okmok (Dean and others, 1998; Dehn and others, 2000), by using a wider range of criteria to determine whether a pixel is a volcanic thermal anomaly or noise. The AVHRR images provide a snapshot of the thermal state of the volcano at that moment in time (fig. 2). The Okmok II algorithm automatically discards cloudy, daytime, and noisy images and then ascertains the apparent temperature of the hottest anomalous pixel in each image, as well as the accompanying background temperature. For the purposes of this paper it is assumed that the hottest pixel includes the summit of Augustine.

Thermally anomalous pixels were also manually identified in 526 images between January 1 and April 30, 2006, by the Alaska Volcano Observatory (AVO) as part of the twice-daily remote-sensing monitoring routine (Bailey and others, this volume). The number is much higher than determined by

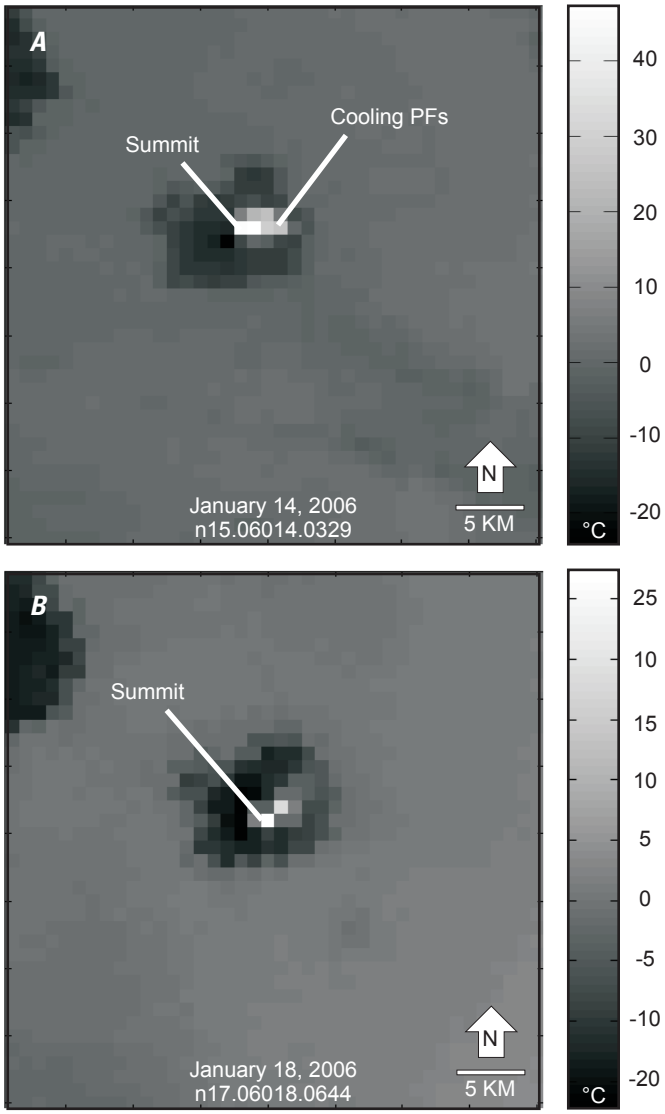

Figure 2. Selected band 3 (thermal infrared; 3.55-3.93 µm) AVHRR data over Augustine Volcano in January 2006 showing thermal anomalies at the summit of Augustine, as well as cooling pyroclastic flows. Both images are north oriented to the top, scalebar is in degrees Celsius (°C), the image identification numbers are noted on the bottom. *A*, January 14 at 03.29 UTC, zenith angle is 27°. *B*, January 18 at 0644 UTC, zenith angle is 42°.

the Okmok algorithm due to the fact that the Okmok algorithm excludes daytime, cloudy, or noisy images that an analyst can still use. For each of the images the number of hot pixels was recorded. This provides an indication of the activity that has occurred, taking into account the whole volcano. Small numbers of pixels with elevated temperatures generally suggest summit activity, whereas larger numbers can indicate cooling lava flows or pyroclastic deposits. However, increases in the number of hot pixels observed are only significant if they are large; with increasing zenith angle, pixels start to overlap, increasing the chance of a hotspot stretching across multiple pixels. In addition, even at lower zenith angles a hotspot can occasionally be on the border of two pixels, thus being reported in two or more pixels instead of one.

Radiative Thermal Flux and Total Radiated energy

The radiant temperature detected by AVHRR is a function of the sensor's field of view (FOV). It is integrated over the entire area of the pixel and can not directly reflect the temperature of the hottest volcanic material except in the highly unlikely event that such material homogenously occupies the whole pixel. This means that estimation of the volcanic temperature requires the simultaneous determination of the proportions of ground surface at various temperatures (Harris and others, 1997; Francis and Rothery, 2000). The radiance received will be affected by atmospheric attenuation and instrumental effects as well as by surface spectral emissivity. To calculate the thermal output from the summit at Augustine, the two-component method (Dozier, 1981; Rothery and others, 1988; Harris and others, 1997; Harris and others, 1998) was used in conjunction with the dataset gathered by the Okmok II algorithm. The manual data was only used to examine the number of hot pixels during the time period investigated. This was done as the Okmok II algorithm maintains constant criteria to determine whether or not a pixel is thermally elevated. This method assumes that a pixel with an elevated temperature (T_{int}) is composed of two parts; a subpixel hotspot at temperature (T_h), occupying a fractional area (p_h), while the remainder is at background temperature (T_{bg}) occupying ($1–p_h$). This assumption allows the temperature and the area covered by each component to be estimated using:

$$L(\lambda, T_{\text{int}}) = p_h L(\lambda, T_h) + (1–p_h)\, L\,(\lambda, T_{bg}) \quad (1)$$

Where L is the Planck function for a blackbody at wavelength λ. This results in three unknowns: the fractional area, the temperature of the hot component, and the temperature of the background. Background temperature can be estimated using the temperatures of surrounding nonanomalous pixels, allowing the remaining two parameters to be calculated if one of them can be assumed or constrained. This work uses an integrated pixel temperature (T_{int}) determined from band 3 (3.55–3.93 µm) and a background temperature determined from band 4 (10.3–11.3 µm). This is done because the peak emittance of the background is closer to the central wavelength of band 4. The two component method is a simplification because a volcano consists of more than one hot and one cold component; however, it provides an accurate first order approximation of the radiative thermal flux. In order for it to work, the ratio of the hot to cold pixel fraction needs to be correct. The fractional area occupied by the hot component was estimated by determining the dome radius; visual observations

indicate this was 110 m, this means approximately 3 percent of each pixel is considered to be at high temperature. Although the size and the shape of the dome changed throughout the course of the eruption, this size estimate provided a plausible ratio of the hot to cold pixel fraction because it is consistent with the satellite derived extrusion rates, which correspond to those observed in the field (Coombs and others, this volume). Having estimated the fractional area of the hot component allowed the temperature of the hot component (T_h) to be calculated. Consequently above-background summit radiative thermal flux (q_r) can be calculated using:

$$q_r = \varepsilon\sigma\tau p_h (T_h^4 - T_{bg}^4) , \quad (2)$$

where τ is the atmospheric transmissivity, σ is the Stefan-Boltzmann constant, and ε is the emissivity of the lava. Atmospheric transmissivity is difficult to account for as it is affected by the total transmissivity of the atmosphere as well as the concentration of volcanic gases above the vent (Dehn and others, 2002). However, due to the fact that the subarctic air is relatively dry, the effect of transmissivity only has a small effect on the absolute temperature values. Emissivity in the relevant wavelengths is assumed to be 0.9, an accepted value for andesitic lavas (Salisbury and D'Aria, 1992). The radiant thermal flux represents the average thermal flux integrated over the entire pixel. No correction for the pixel size is made, as the precise geometry of the edifice changes and the viewing geometry of the satellite is hard to constrain.

Using radiative thermal flux to monitor activity will result in underestimates of total energy flux at a volcano because other sources of heat loss such as convection, conduction, evaporation of rainfall, and hydrothermal circulation are ignored (Francis and Rothery, 2000). Radiative thermal flux is just one component of the total heat loss, however since it is the largest is provides a good proxy for the thermal state, and thus activity level, of a volcano. The total radiated energy was calculated by using the trapezoidal method of integration.

Seismic Tremor Data

Reduced displacement (D_r) is a low sample rate measure of seismic amplitude. It is widely used to normalize volcanic tremor recorded at varying distances from a volcano to a common scale and to allow comparisons between eruptions. It is a simple measure equal to the sustained root mean square (rms) ground displacement corrected for geometric spreading (Aki and Koyanagi, 1981). Site amplification can influence the results, but the order of magnitude scaling typically used with reduced displacement minimizes the influence of a constant scale factor.

For this study we use D_r calculated from channel HHZ (the vertical component) of station AU13 (59.3464ºN, 153.4341ºW). AU13 was chosen because it had a high signal-to-noise ratio, had few data gaps, remained on scale through the eruption, and was generally representative of D_r from other stations at Augustine. The sensor was a Guralp CMG-6TD (30 s) installed shortly before the eruption. This station was located 1.8 km from the summit (fig. 1). Because the station is within a few wavelengths of the source region beneath the summit, we use the body wave formulation of reduced displacement first presented by Aki and Koyanagi (1981). The original expression, formulated for paper records, is:

$$D_r = \frac{A}{2\sqrt{2}} \cdot \frac{r}{M} \quad (3)$$

where A is the peak-to-peak amplitude of the raw seismogram and the factor of estimates its root-mean-square value from the peak-to-peak measure. The source-to-receiver distance r, is the salient part of the expression which "reduces" the displacement to a common value. The magnification value, M, scales the seismogram from arbitrary units to true ground displacement. Although A is measured from raw seismic data, M, is frequency dependent. In this formulation M should be chosen at a frequency which best matches the tremor, thus introducing a frequency dependence to the reduced displacement expression.

The approach used in this study is true to the original definition of reduced displacement but benefits from digital processing techniques. In lieu of applying a frequency-dependent magnification factor, we use seismic data that have been corrected for instrument response and integrated from velocity to displacement. We calculate the root mean square of this signal directly. Although this is a more brute force approach, it can be written simply as:

$$D_r = RMS\,(X) \cdot r \quad (4)$$

where X is the instrument-corrected displacement record. In practice this is comparable to using the original formulation of Aki and Koyanagi (1981) without the frequency assumption introduced by the magnification factor. Here we calculate D_r on 30-minute windows of data, band-pass filtered for a frequency range of 0.5 to 8 Hz. The filter preserves the dominant frequencies of tremor, volcanic earthquakes, and rock falls while minimizing both the low-frequency microseism band and high-frequency wind noise. The wide frequency window is consistent with the use of reduced displacement in many monitoring environments.

It should be noted that this formulation for reduced displacement varies from a modified version used operationally by AVO (see McNutt and others, this volume). The operational version measures seismic amplitude in a narrow band around the dominant frequency of the signal. To make use of more distant stations, this approach also uses a geometric spreading term consistent with surface waves (Fehler, 1983). Because of the broader band approach, body wave decay term, and the use of stations close to the summit, values presented here are generally higher than those of McNutt and others (this volume). The discrepancy is inherent in the different approximations

required to reduce complex seismic records to a simple metric, such as reduced displacement. However it is precisely such simplifications that allow quantitative comparisons between different eruptive episodes.

Analyses and Results

Thermal emissions and reduced displacement data plots were made using data spanning the entire eruption. The coeruptive data were examined in detail and additional analyses were performed on selected subsets.

Thermal Imagery

Summit Radiative Thermal Flux and Total Radiated Energy

The data show three broad peaks during which the summit radiative thermal flux rose above the average eruption background value of less than 10^8 W (figs. 3*A*, 4*A*). An additional minor spike is visible near the end of April. On the basis of the thermal imagery, the total energy output from the summit region of Augustine between January 1 and April 30, 2006, is 2.15×10^{16} J. The thermal flux increases appear to occur predominantly in three sequences as indicated by three time periods showing a distinct increase in slope on the cumulative energy output plot (fig. *5A*).

Although thermal anomalies (figs. *3A, 4A*) are observed prior to the start of the explosive activity on January 11, thermal flux then was lower, not exceeding $1x10^8$ W. The first main spike in thermal flux is not until January 13 at 13.27 h UTC, almost 48 hours after the initial explosions, when the summit thermal flux reaches 1.1×10^{10} W. This spike is then followed by two smaller but slightly broader spikes on January 14 and 17. On January 18 another large narrow spike of 8.2×10^9 W can be observed.

After January 20, radiative thermal flux again falls below $1x10^8$ W, until January 26 after which it quickly starts to rise. A small spike of 7.2×10^9 W can be seen on January 28, coincident with the four explosions that occurred during this phase. A spike of 1.6×10^{10} W is observed on February 3, after this the thermal flux tapers off quickly until February 13. Minor spikes of 1.3×10^{10} W and 6.8×10^9 W are seen on February 8 and 13.

Summit thermal flux starts to increase again on February 20, this time ramping up more slowly to a maximum of 1.7×10^{10} W on March 8. Numerous minor spikes are visible, including ones on February 26, March 1, and March 11, which reach 8.2×10^9 W, 1.5×10^{10} W, and 1.3×10^{10} W, respectively.

A small spike of 2.4×10^9 W, with some minor ramping up to this peak, can be seen on March 23. Another anomalous single spike with some minor increases beforehand can be observed in the radiative thermal flux towards the end of April, spiking on April 19 at 4.0×10^9 W.

Number of Hot Pixels

The number of hot pixels (N_{HP}) observed (fig. 3*B*) shows three sequences during which their number increases from a background value of approximately 2 during the eruption to more than 10. The timing of these sequences coincides with the spikes observed in the thermal data. There is also a remarkable correlation between N_{HP} and the reduced displacement values: the number of days that both are elevated is almost equal, whereas the radiative thermal flux increases have longer durations (broader peaks).

The number of hot pixels observed starts to increase on January 13, reaching an initial peak of 18 on January 14. N_{HP} then decreases again only to peak on January 19 at 10. The number of hot pixels does not exceed 2 between January 20 and January 28. After this a sharp increase can be observed, with the series maximum of 37 pixels observed on January 28 at 0615 h UTC. From January 29 onwards N_{HP} remains high, varying between 6 and 30 until February 7. Throughout the rest of February values remain between 1 and 9 pixels per image. March 1 sees an increase to 15 pixels; however, this value then drops to 2 pixels per image until March 5. After this N_{HP} observed increases again, although less sharply than during the previous phase of increases, only to peak at 35 on March 8. A slow decrease after this continues until March 30, after which values do not exceed 6, but most images only show 2 anomalous pixels.

Reduced Displacement

In general the reduced displacement (fig. *3C*) shows a trend similar to those for thermal emissions data and the number of hot pixels observed; there are three distinct intervals when reduced displacement rises above the average eruption background level of 10 cm^2.

Reduced displacement shows a number of minor peaks above background level before the explosions on January 11. On January 11 the peak value reached 417 cm^2. Levels then dropped back to background levels until January 13 when the highest reduced displacement value recorded at station AU13 during the eruption, 1,680 cm^2, was observed. Additional spikes are seen on January 14, but they do not exceed 500 cm^2. Another major spike is seen on January 17, this peaks at 1,034 cm^2. Each of these high reduced displacement values coincides with one of the 9 recorded explosions during this time. Cumulative reduced displacement values (fig. 5*A*) show very sharp step-like increases in the values associated with the spikes observed in the 30 minute data.

After January 17 reduced displacement does not rise above 100 cm^2 until January 28. The cumulative values reflect this as a very shallow sloping increase. Four more explosions occurred on January 28; however, reduced displacement peaks at only 395 cm^2. Reduced displacement values remain high even after the explosions cease, peaking on January 30 and 31 and February 5 at 381 cm^2, 597 cm^2, and 536 cm^2,

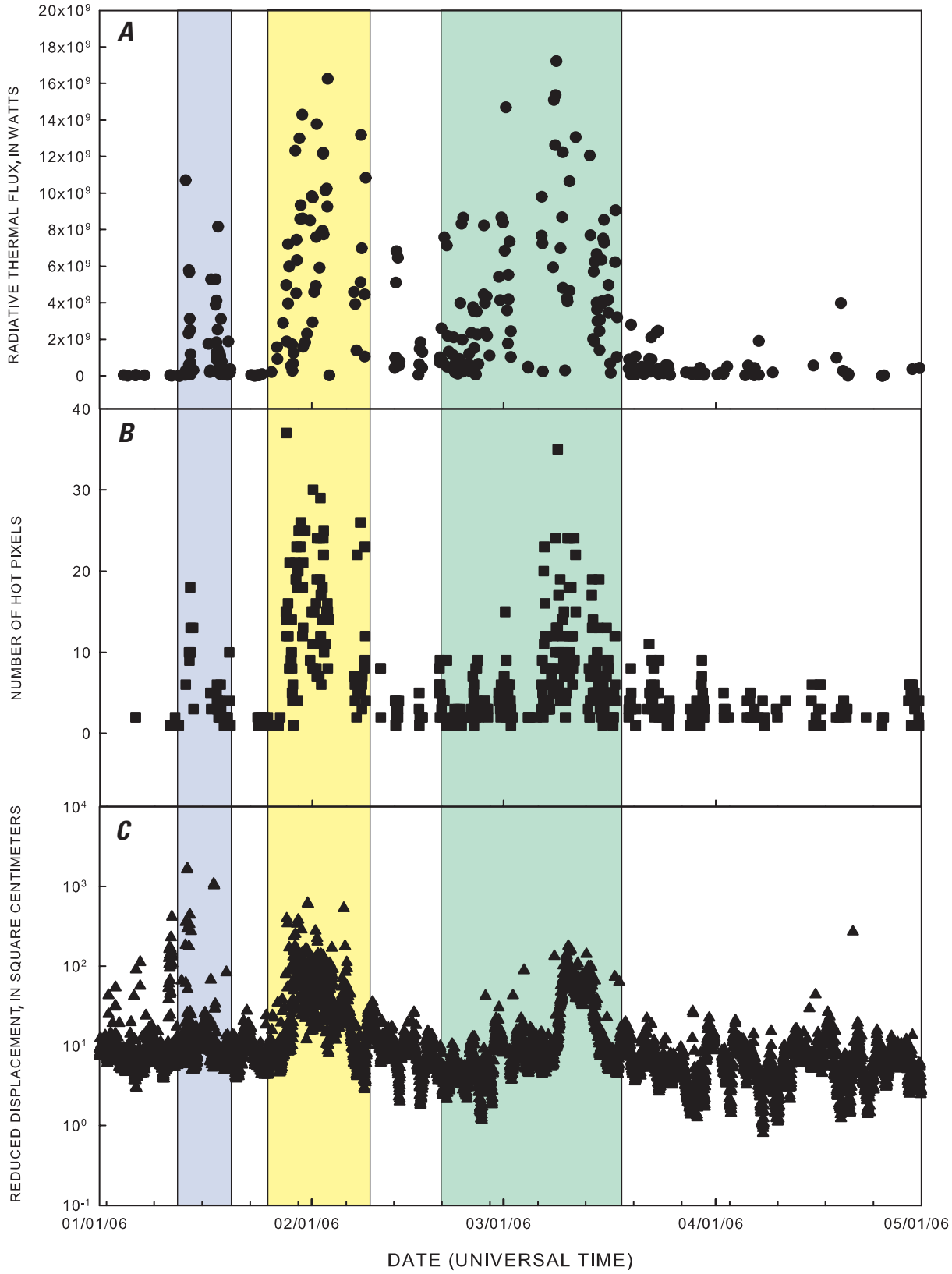

Figure 3. Summary of satellite thermal data collected from Augustine between January 1, 2006, and April 30, 2006. *A*, Summit thermal emissions; *B*, number of hot pixels per satellite image; and *C*, reduced displacement. All three data sets show three contemporaneous peaks. Please note the logarithmic scale on the y-axis of plot *C*. The colored bands indicate the three sequences of increased summit radiative thermal flux.

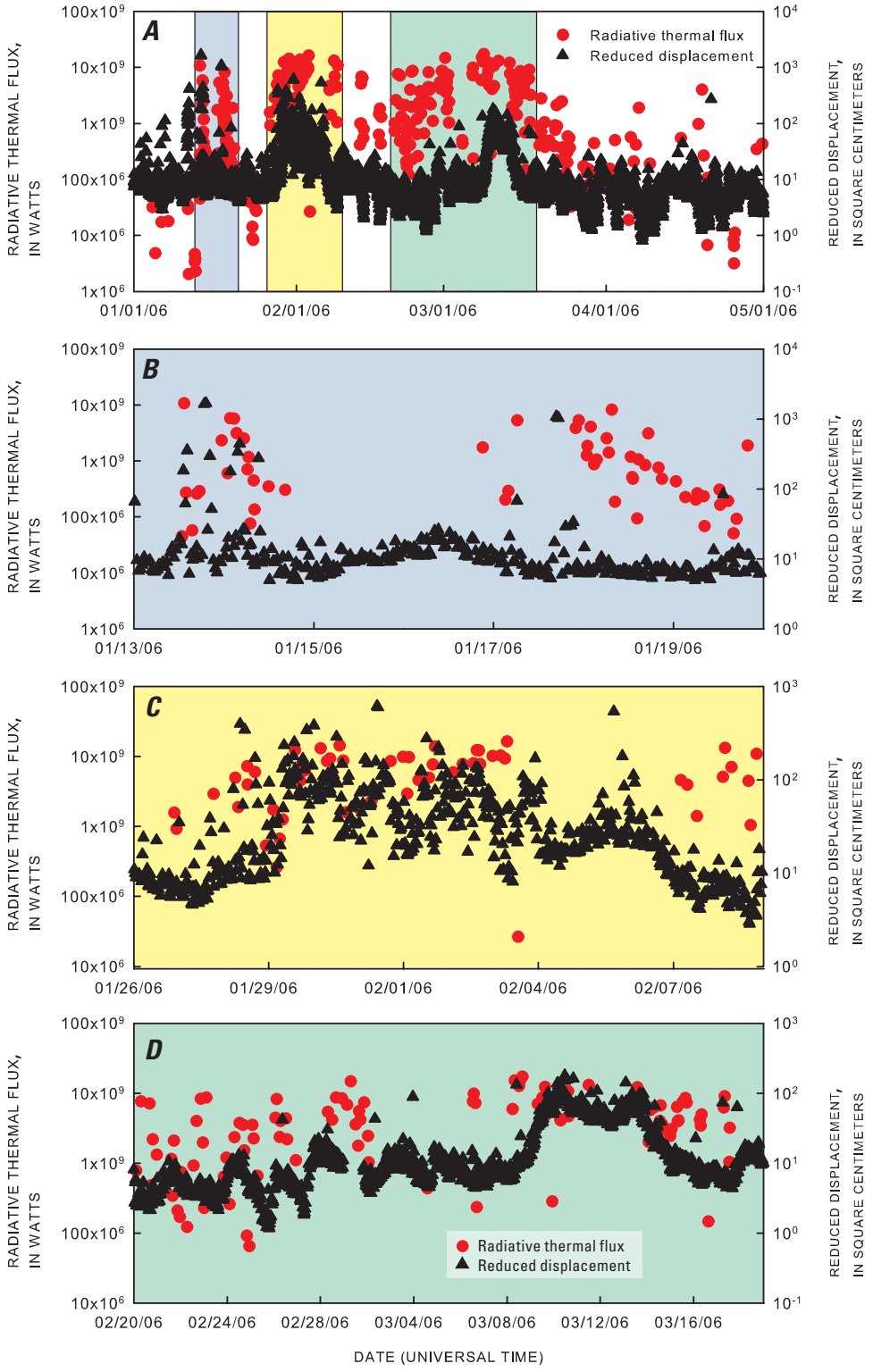

Figure 4. Summit thermal emissions (red) and reduced displacement (black) from Augustine Volcano as observed between January 1, 2006, and April 30, 2006. *A*, January 1, 2006, and April 30, 2006. The graph shows three areas where increases in thermal emissions and reduced displacement coincide. The colored bands indicate the three sequences of increased summit radiative thermal flux. *B*, First sequence of increased thermal emissions. *C*, Second sequence of increased thermal emissions. *D*, Third sequence of increased thermal emissions.

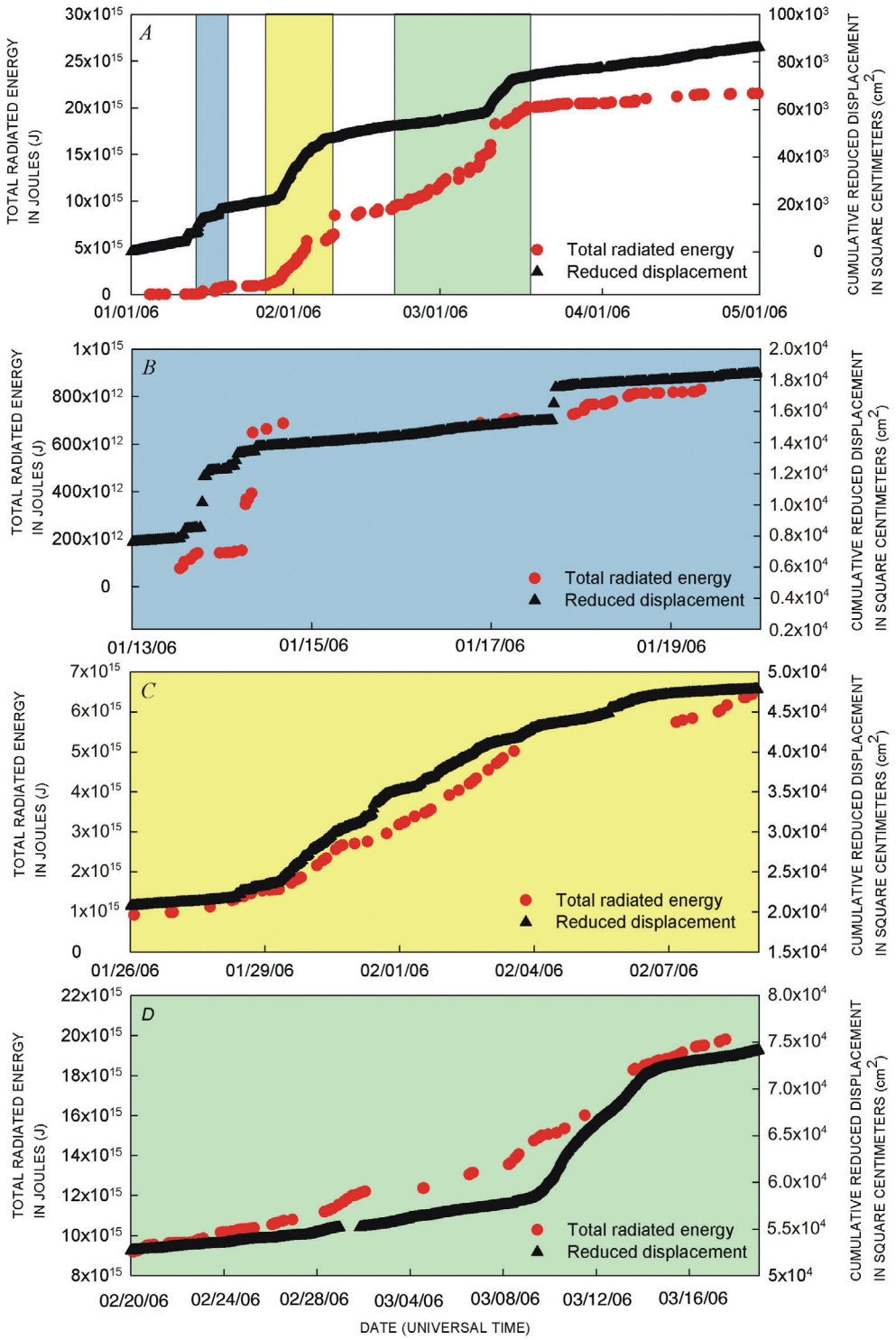

Figure 5. Total thermal energy output (red) and cumulative reduced displacement values (black) at Augustine Volcano between January 1, 2006, and April 30, 2006. *A*, January 1, 2006, until April 30, 2006. The graph shows the three phases as indicated by the colored bands. Note the differences in shape of the graph between phase 1 and 2 and phase 3. *B*, First sequence of increased thermal emissions; increases in thermal energy output postdate increases in reduced displacement. *C*, Second sequence of increased thermal emissions; increases in thermal energy output and reduced displacement occur almost contemporaneously. *D*, Third sequence of increased thermal emissions; increases in thermal energy output precede increases in reduced displacement.

respectively. This is reflected in the cumulative values in a steady increase in the slope.

Between February 7 and March 3 reduced displacement barely rose above background values, even at a maximum not exceeding 50 cm^2. Two minor peaks are visible on February 26 and March 2, but these do not rise to more than 42 cm^2. These background values are represented in the cumulative plot as a shallowly sloping line. Another single peak in the reduced displacement values is observed on March 8, reaching 133 cm^2. After this peak values drop to background levels only to slowly ramp up to a maximum of 179 cm^2 on March 10. Activity remains high, continuously exceeding 40 cm^2 with a minor peak on March 13 of 141 cm^2. The increase visible in the 30-minute reduced displacement values between March 8 and March 14 and is attributed to a continuous seismic tremor. After March 14 activity returns to background levels, manifested in the cumulative plot as a shallowly sloping line.

Combined Analysis of Thermal and Seismic Tremor Data

Two main types of behaviour are observed: (1) radiative thermal flux and reduced displacement have corresponding peaks, or (2) radiative thermal flux and reduced displacement do not have corresponding peaks (fig. 4). In general, peaks in the reduced displacement data and number of hotspots observed are much narrower in time than those of the radiative thermal flux.

The first explosions that occurred on January 11, 2006, did not produce a corresponding thermal signal (fig. 4*A*). The first time span that shows coincident increases in radiative thermal flux and reduced displacement is between January 13 and January 19. During this first peak in thermal output, high reduced displacement values coincide with the 9 recorded explosions (Petersen and others, 2006). The cumulative plot (figs. 5*A*, *B*) clearly shows that the total radiated energy did not increase until after the reduced displacement values had started to increase.

The second period when radiative thermal flux and reduced displacement display corresponding increases is between January 26 and February 6. In this case, the summit thermal flux started to increase coincident with the increase in reduced displacement (fig. 4*C*) and remained high after the reduced displacement has died down. High reduced displacement values do not correspond solely to explosions during this time, suggesting a contribution from other sources such as rockfalls.

During the third peak in summit radiative thermal flux, the rise of total radiated energy preceded increases in reduced displacement (figs. 4*D*, 5*D*). There is a very large jump in the total thermal energy output that coincides with the start of the increase in reduced displacement. Additional corresponding increases in thermal emissions and reduced displacement occur between March 8 and March 14. Reduced displacement increased at this time due to continuous seismic tremor. There are no directly corresponding peaks between the radiative thermal flux and the reduced displacement.

Interpretation

On the basis of the data there appear to be three sequences of increased summit radiative thermal flux—January 13–19 (figs. 4B, *5B*), January 26–February 8 (figs. 4*C*, 5*C*), and February 20–March 18 (figs. 4*D*, 5*D*). All three sequences are also characterized by increased numbers of hot pixels and increased reduced displacement; therefore, each of these three sequences has been interpreted as a period of lava extrusion (table 1). The first two sequences incorporate explosive activity whereas the last sequence is purely effusive. Figure 6 illustrates the changes occurring at the summit during these three sequences. There does not appear to be a correlation between the type of magma erupted (low and high silica andesite) as described in Coombs and others (this volume) and the seismic or thermal activity described here.

Sequence 1 (January 13–19)

The first sequence, which occurred during the explosive phase as identified by Coombs and others (this volume) and Power and Lalla (this volume), was characterized by high average reduced displacement values and low average thermal energy output compared to the other two sequences. However,

Table 1. Characteristics of each of the three sequences of increased thermal emissions.

Sequence	Dates	Duration (days)	Total radiated energy (x 10^{15} J)	Average radiated energy per day (x 10^{14} J)	Number of explosive events	Total reduced displacement (x 10^4 cm^2)	Average reduced displacement/day (x 10^3 cm^2)
1	01/13/06-01/19/06	7	0.82	1.3	7	1.09	1.57
2	01/26/06-02/08/06	14	5.53	4.01	4	2.71	1.98
3	02/20/06-03/18/06	27	10.60	4.18	0	2.14	0.75

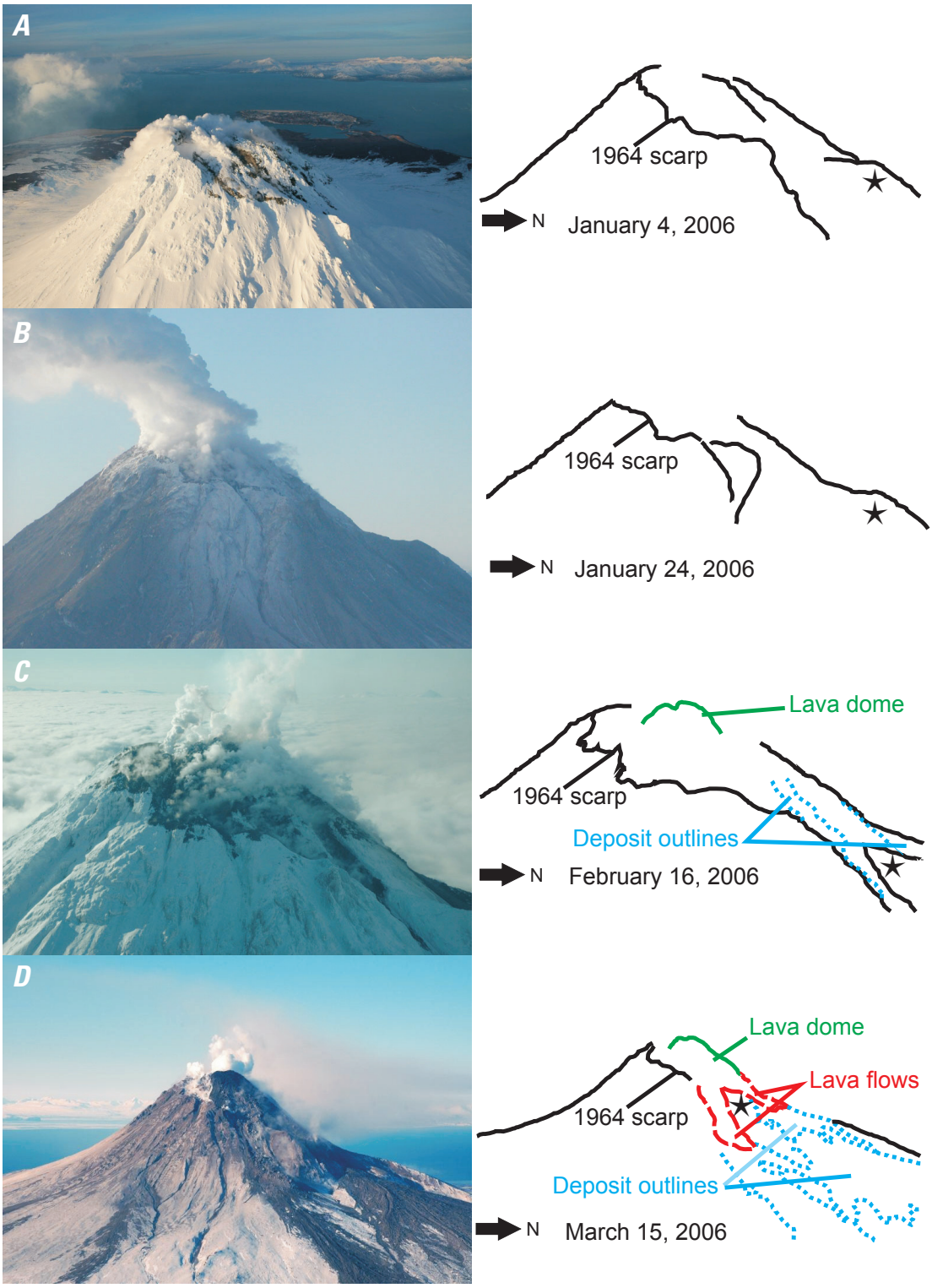

Figure 6. Pictorial time series of changes at the dome throughout the 2006 eruption of Augustine Volcano. The star in each image indicates the location of a feature known as "the Cleaver" for comparison purposes. *A*, The dome prior to magma extrusion, January 4, 2006 (AVO image by M. Coombs). *B*, January 24, 2006 (AVO image by J. Schaefer). *C*, The dome on February 16 after the second sequence of increased radiative thermal flux. (AVO image by R.G. McGimsey). *D*, The dome on March 15 2006, towards the end of the last phase of dome growth (AVO image by T. Plucinski).

the average thermal energy output still significantly exceeded background values. During this sequence a significant amount of mechanical energy was expended without bringing much hot material to the surface. In addition, the fact that increases in reduced displacement preceded increases in thermal energy output further suggests that this sequence was mainly conduit-clearing explosive activity accompanied by intermittent extrusion of lava and numerous pyroclastic flows. The number of hot pixels observed during this sequence did increase, suggesting both extrusion at the summit and the occurrence of pyroclastic flows. During this first sequence the volcano was still inflating, suggesting that the rate of magma accumulation at depth was greater than eruption rates. This interpretation is consistent with visual information obtained on overflights of the volcano; Coombs and others (this volume) reported a small new lava dome on January 16 (fig. 7) and fresh glass shards in ash samples on January 14. However, this small new dome was destroyed on January 17 by an explosion, so there was little change to the summit area compared to before the start of the sequence (figs. 6*A*, *B*). Coombs and others (this volume) list the explosive phase as the most voluminous at $30x10^6$ m^3 dense rock equivalent; however, the majority of this was extruded towards the end during January 27–28, which in this study falls into sequence 2. A lot of the material extruded during sequence 1 was in the form of tephra, which being cold is not accounted for in this paper. Large amounts of tephra in the form of ash in a plume could attenuate the thermal signal, although we think that this is not the case here as even during the almost continuous ash emissions observed during the start of sequence 2 (Coombs and others, this volume) saturation of the sensors occurred.

Sequence 2 (January 26–February 8)

The second sequence was contemporaneous with the redefined continuous phase of the eruption (Coombs and others, this volume). High thermal energy output in combination with high reduced displacement values (table 1) during this sequence lead to the interpretation that this was a significant period of lava extrusion and dome growth. The absence of explosive activity after January 28 indicates that an open conduit to the surface had been established. The fact that reduced displacement values remained high after the explosive activity ceased on January 28 suggests that at this time there was also major migration of gas, fluid, and magma occurring within the edifice. This is confirmed by the thermal radiative flux which indicates significant dome growth and high extrusion rates. It is important to note that the high radiative flux is due to a combination of heat from the dome and from pyroclastic deposits, which are an indirect indicator of dome growth. This would suggest that there was significant movement of magma, as was also reflected in the reduced displacement values. The rapid dome growth would have resulted in oversteepening of the dome, resulting in rockfalls. These rockfalls also form a contribution to the reduced displacement signal. Figures 6*B* and *C* illustrate the visual changes that occurred at the summit during this sequence; the new dome is clearly visible, as

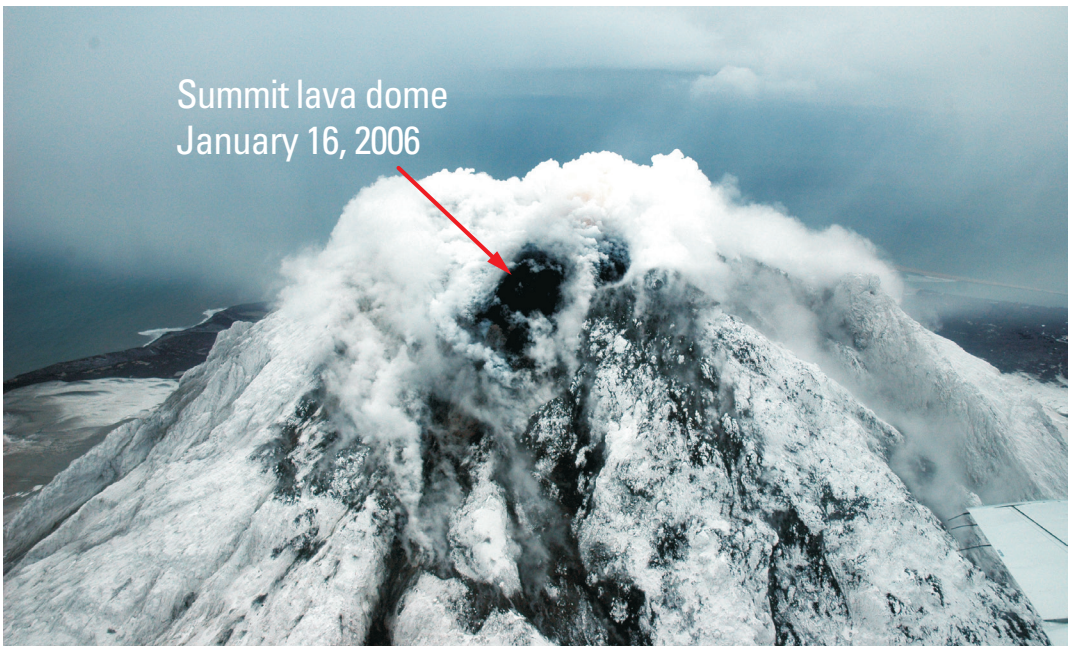

Figure 7. Augustine Volcano summit lava dome on January 16, 2006. Arrow points at the dome (AVO image by R.G. McGimsey).

are deposits from pyroclastic and block and ash flows. The emplacement of these deposits is reflected in the significant increase of the number of hot pixels recorded during this sequence. This sequence coincided with a period of deflation (Cervelli and others, this volume), also implying significant growth of the lava dome. It is likely that fresh magma was being erupted at this time, after the explosive behavior of both the first sequence and the January 28 explosions had cleared the vent.

Sequence 3 (February 20–March 18)

The third sequence, which occurred during the so-called hiatus and effusive phase (Coombs and others, this volume), was characterized by (1) high thermal energy output and (2) reduced displacement that was elevated but lower than during earlier eruptive phases (table 1). During the first part of this sequence little seismic energy was generated, suggesting that an open conduit to the surface had been established. The high radiative thermal flux values indicate there was significant extrusion of magma, not just to the dome but also to the two lava flows that formed to the north during this time. The peak thermal emissions during this sequence coincide with a period of deflation, which suggests that extrusion rates were greater than magma supply rates. This significant episode of dome growth would again have resulted in oversteepening of the dome and rockfalls, which are reflected in the reduced displacement signal. The radiative thermal flux peaks at the start of continuous tremor that occurred from March 8 until March 14. This suggests that towards the end of the eruption there was significant migration of gas, fluids, and magma, even though radiative thermal flux declines during this time. The movement of magma is reflected in the GPS data which indicate that at this time the edifice starts to inflate again (Cervelli and others, this volume). Visual observations (figs. 6*C*, *D*) show that during this sequence two short blocky lava flows were extruded and there were additional pyroclastic and block and ash flows. These lava flows and pyroclastic deposits are reflected in the number of hot pixels observed, which increased significantly during this time. Traditionally the end of lava effusion is estimated based on the time of the last image with saturated pixels in band 3; saturation generally occurs due to lava incandescence (Harris and others, 1997). Although this is a valid assumption for basaltic activity, dome growth can occur endogenously, thus not saturating the thermal signal. The last image with saturated pixels at Augustine was recorded on March 15; however, an image close to saturation was observed on March 17. Data were unavailable on March 18, whereas the temperatures observed on March 19 were significantly cooler. This suggested that extrusion of lava ceased between March 15 and 18; after this the thermal flux slowly decreased, indicating cooling of the extruded material. This is consistent with FLIR observations made on March 15 and March 26 (Wessels and others, this volume).

Implications for Future Monitoring

Although remote sensing data are important in the operational monitoring of active and potentially active volcanoes, there is a limit to the amount of information they can provide. To gain the most information regarding a volcanic system, thermal signatures need to be related to other observable activity. This will increase understanding of the processes occurring on the ground. This is particularly important for remote volcanoes that are monitored solely by remote techniques.

Analysis of the 2006 Augustine data has shown that summit thermal emissions and reduced displacement exhibit patterns that can be tied to specific types of volcanic behavior. It was found that high thermal energy output with corresponding high reduced displacement values indicate extrusion of magma whereas low thermal energy output values with correspondingly high reduced displacement values are associated with explosive behavior. The fact that most of the extrusion seemed to generate relatively little mechanical seismic energy suggests that after the explosive activity subsided an open conduit was established.

No reliable exploitable predictive trend that can be extrapolated to other dome building volcanoes has been found in the 2006 eruption Augustine radiative thermal flux. This is probably due to stochastic variations, as well as other factors such as the temporal coverage of the satellite data and local weather conditions.

This study highlights the importance of multiparametric synergistic studies. The joint analysis of both data sets is consistent with three sequences of lava dome extrusion. Interpretations of thermal emissions and correlations with other datasets can be optimized by monitoring thermal emissions at increased spatio-temporal resolution. Although AVHRR can be used to constrain the magnitude of the activity occurring at a volcano, it can not provide detailed data regarding the eruptive state of a volcano unless supplementary datasets (particularly continuous seismic data) are available. However, the temporal coverage in the Alaska-Aleutian-Kamchatka region makes AVHRR an invaluable tool for monitoring the gross behavior of hazardous volcanoes.

Acknowledgments

The authors would like to acknowledge the Alaska Volcano Observatory—a cooperative program between the U.S. Geological Survey Volcano Hazards Program, the Geophysical Institute at the University of Alaska Fairbanks, and the Alaska Division of Geological and Geophysical Surveys. A grant from the Geological Society of London funded Saskia M. van Manen's visit to AVO while the paper was being completed. In addition we would like to thank R. Wessels and M. Patrick for their helpful reviews.

References Cited

Aki, K., Christofferson, C., and Husebye, E.S., 1977, Determination of the three-dimensional seismic structure of the lithosphere: Journal of Geophysical Research, v. 82, p. 277–296.

Aki, K., and Koyanagi, R., 1981, Deep volcanic tremor and magma ascent mechanism under Kilauea, Hawaii: Journal of Geophysical Research, v. 86, no. NB8, p. 7095–7109.

AVO Remote Sensing Team, 2000, Manual for Satellite Monitoring of Volcanoes: Fairbanks, Alaska, Alaska Volcano Observatory, p. 47.

Bailey, J.E., Dean, K.G., Dehn, J., and Webley, P.W., 2010, Integrated satellite observations of the 2006 eruption of Augustine Volcano, *in* Power, J.A., Coombs, M.L., and Freymueller, J.T., eds., The 2006 eruption of Augustine Volcano, Alaska: U.S. Geological Survey Professional Paper 1769 (this volume).

Benoit, J.P., McNutt, S.R., and Barboza, V., 2003, Duration-amplitude distribution of volcanic tremor: Journal of Geophysical Research—Solid Earth, v. 108, no. B3, p. 15.

Cervelli, P.F., Fournier, T.J., Freymueller, J.T., Power, J.A., Lisowski, M., and Pauk, B.A., 2010, Geodetic constraints on magma movement and withdrawal during the 2006 eruption of Augustine Volcano, *in* Power, J.A., Coombs, M.L., and Freymueller, J.T., eds., The 2006 eruption of Augustine Volcano, Alaska: U.S. Geological Survey Professional Paper 1769 (this volume).

Coombs, M.L., Bull, K.F., Vallance, J.W., Schneider, D.J., Thoms, E.E., Wessels, R.L., and McGimsey, R.G., 2010, Timing, distribution, and volume of proximal products of the 2006 eruption of Augustine Volcano, *in* Power, J.A., Coombs, M.L., and Freymueller, J.T., eds., The 2006 eruption of Augustine Volcano, Alaska: U.S. Geological Survey Professional Paper 1769 (this volume).

Dean, K., Servilla, M., Roach, A., Foster, B., and Engle, K., 1998, Satellite monitoring of remote volcanoes improves study efforts in Alaska: Eos (Transactions American Geophysical Union), v. 75, no. 35, p. 413.

Dehn, J., Dean, K., and Engle, K., 2000, Thermal monitoring of North Pacific volcanoes from space: Geology, v. 28, no. 8, p. 755–758.

Dehn, J., Dean, K.G., Engle, K., and Izbekov, P., 2002, Thermal precursors in satellite images of the 1999 eruption of Shishaldin Volcano: Bulletin of Volcanology, v. 64, no. 8, p. 525–534.

Dozier, J., 1981, A method for satellite identification of surface temperature fields of subpixel resolution: Remote Sensing of Environment, v. 11, no. 3, p. 221–229.

Endo, E.T., and Murray, T., 1991, Real-time seismic amplitude measurement (RSAM)—A volcano monitoring and prediction tool: Bulletin of Volcanology, v. 53, no. 7, p. 533–545.

Fehler, M., 1983, Observations of volcanic tremor at Mount St Helens Volcano: Journal of Geophysical Research, v. 88, no. NB4, p. 3476–3484.

Fink, J.H., and Griffiths, R.W., 1998, Morphology, eruption rates, and rheology of lava domes—Insights from laboratory models: Journal of Geophysical Research—Solid Earth, v. 103, no. 1, p. 527–545.

Francis, P., and Rothery, D.A., 2000, Remote sensing of active volcanoes: Annual Review of Earth and Planetary Sciences, v. 28, p. 81–106.

Galindo, I., and Dominguez, T., 2002, Near real-time satellite monitoring during the 1997–2000 activity of Volcan de Colima (Mexico) and its relationship with seismic monitoring: Journal of Volcanology and Geothermal Research, v. 117, no. 1-2, p. 91–104.

Harris, A.J.L., Butterworth, A.L., Carlton, R.W., Downey, I., Miller, P., Navarro, P., and Rothery, D.A., 1997, Low-cost volcano surveillance from space—Case studies from Etna, Krafla, Cerro Negro, Fogo, Lascar and Erebus: Bulletin of Volcanology, v. 59, no. 1, p. 49–64.

Harris, A.J.L., Flynn, L.P., Keszthelyi, L., Mouginis-Mark, P.J., Rowland, S.K., and Resing, J.A., 1998, Calculation of lava effusion rates from Landsat TM data: Bulletin of Volcanology, v. 60, no. 1, p. 52–71.

Jacobs, K.M., and McNutt, S.R., 2010, Using seismic *b*-values to interpret seismicity rates and physical processes during the preeruptive earthquake swarm at Augustine Volcano 2005–2006, *in* Power, J.A., Coombs, M.L., and Freymueller, J.T., eds., The 2006 eruption of Augustine Volcano, Alaska: U.S. Geological Survey Professional Paper 1769 (this volume).

Julian, B.R., 1994, Volcanic tremor: nonlinear excitation by fluid-flow: Journal of Geophysical Research-Solid Earth, v. 99, no. B6, p. 11859–11877.

Lahr, J.C., Chouet, B.A., Stephens, C.D., Power, J.A., and Page, R.A., 1994, Earthquake classification, location and error analysis in a volcanic environment: implications for the magmatic system of the 1989–1990 eruptions of Redoubt volcano, Alaska: Journal of Volcanology and Geothermal Research, v. 62, no. 1–4, p. 137–152.

Larsen, J.F., Nye, C.J., Coombs, M.L., Tilman, M., Izbekov, P., and Cameron, C., 2010, Petrology and geochemistry of the 2006 eruption of Augustine Volcano, *in* Power, J.A., Coombs, M.L., and Freymueller, J.T., eds., The 2006 eruption of Augustine Volcano, Alaska: U.S. Geological Survey Professional Paper 1769 (this volume).

Latter, J.H., 1979, Volcanological observations at Tongariro National Park—2, Types and classification of volcanic earthquakes 1976–1978: New Zealand, Department of Scientific and Industrial Research Geophics Division Report no. 150., p. 60.

Lee, C.-W., Lu, Z., Jung, H. S, Won, J.-S., and Dzurisin, D., 2010, Surface deformation of Augustine Volcano, 1992–2005, from multiple-interferogram processing using a refined small baseline subset (SBAS) interferometric synthetic aperture radar (InSAR) approach, *in* Power, J.A.,

Coombs, M.L., and Freymueller, J.T., eds., The 2006 eruption of Augustine Volcano, Alaska: U.S. Geological Survey Professional Paper 1769 (this volume).

Malone, S.D., Boyko, C., and Weaver, C.S., 1983, Seismic precursors to the Mount St. Helens—Eruptions in 1981 and 1982: Science, v. 221, no. 4618, p. 1376–1378.

McNutt, S.R., 1994, Volcanic tremor amplitude correlated with eruption explosivity and its potential use in determining ash hazards to aviation: U.S. Geological Survey Bulletin 2047, p. 377–385.

McNutt, S.R., 2005, Volcanic seismology: Annual Review of Earth and Planetary Sciences, v. 33, p. 461–491.

McNutt, S.R., Tytgat, G., Estes, S.A., and Stihler, S.D., 2010, A parametric study of the January 2006 explosive eruptions of Augustine Volcano, using seismic, infrasonic, and lightning data, *in* Power, J.A., Coombs, M.L., and Freymueller, J.T., eds., The 2006 eruption of Augustine Volcano, Alaska: U.S. Geological Survey Professional Paper 1769 (this volume).

Miller, T.P., and Casadevall, T.J., 1998, Volcanic Ash, Hazards to Aviation, *in* Sigurdsson, H., Houghton, B., McNutt, S.R., Rymer, H., and Stix, J., eds., Encyclopedia of Volcanoes: San Diego, Academic Press, p. 915–930.

Miller, T.P., McGimsey, R.G., Richter, D.H., Riehle, J.R., Nye, C.J., Yount, M.E., and Dumoulin, J.A., 1998, Catalog of the historically active volcanoes of Alaska: U.S. Geological Survey Open-File Report 98-582, p. 104.

Mouginis-Mark, P.J., Crisp, J.A., and Fink, J.H., 2000, Remote sensing of active volcanism: Washington, D.C., American Geophysical Union, 272 p.

Neuberg, J., and O'Gorman, C., 2002, A model of the seismic wavefield in gas-charged magma—Application to Soufriere Hills Volcano, Montserrat, *in* Druitt, T.H., and Kokelaar, B.P., eds., The Eruption of Soufriere Hills Volcano, Montserrat, from 1995 to 1999: Geological Society of London, p. 603–609.

Nye, C.J., Keith, T.E.C., Eichelberger, J.C., Miller, T.P., McNutt, S.R., Moran, S., Schneider, D.J., Dehn, J., and Schaefer, J.R., 2002, The 1999 eruption of Shishaldin Volcano, Alaska—Monitoring a distant eruption: Bulletin of Volcanology, v. 64, no. 8, p. 507–519.

Petersen, T., De Angelis, S., Tytgat, G., and McNutt, S.R., 2006, Local infrasound observations of large ash explosions at Augustine Volcano, Alaska, during January 11–28, 2006: Geophysical Research Letters, v. 33, no. 12, p. doi:10.1029/2006GLO26491.

Power, J.A., Nye, C.J., Coombs, M.L., Wessels, R.L., Cervelli, P.F., Dehn, J., Wallace, K., Freymueller, J.T., and Doukas, M.P., 2006, The Reawakening of Alaska's Augustine Volcano: Eos (Transactions American Geophysical Union), v. 87, no. 37, p. 373, 377.

Power, J.A., and Lalla, D.J., 2010, Seismic observations of Augustine Volcano, 1970–2007, *in* Power, J.A., Coombs, M.L., and Freymueller, J.T., eds., The 2006 eruption of Augustine Volcano, Alaska: U.S. Geological Survey Professional Paper 1769 (this volume).

Roach, A.L., Benoit, J.P., Dean, K.G., and McNutt, S.R., 2001, The combined use of satellite and seismic monitoring during the 1996 eruption of Pavlof volcano, Alaska: Bulletin of Volcanology, v. 62, no. 6-7, p. 385–399.

Rothery, D.A., Francis, P.W., and Wood, C.A., 1988, Volcano monitoring using short wavelength infrared data from satellites: Journal of Geophysical Research, v. 93, no. B7, p. 7993–8008.

Salisbury, J.W., and D'Aria, D.M., 1992, Emissivity of terrestrial materials in the 8-14 μm atmospheric window: Remote Sensing of Environment, v. 42, no. 2, p. 83–106.

Shaw, H.R., 1980, The fracture mechanisms of magma transport from the mantle to the surface, *in* Hargraves, R.B., ed., Physics of Magmatic Processes: Princeton, N.J., Princeton University Press, p. 201–264.

Siebert, L., Beget, J.E., and Glicken, H., 1995, The 1883 and late-prehistoric eruptions of Augustine volcano, Alaska: Journal of Volcanology and Geothermal Research, v. 66, no. 1, p. 367–395.

Wallace, K.L., Neal, C.A., and McGimsey, R.G., 2010, Timing, distribution, and character of tephra fall from the 2005–2006 eruption of Augustine Volcano, *in* Power, J.A., Coombs, M.L., and Freymueller, J.T., eds., The 2006 eruption of Augustine Volcano, Alaska: U.S. Geological Survey Professional Paper 1769 (this volume).

Waythomas, C.F., Watts, P., and Walder, J.S., 2006, Numerical simulation of tsunami generation by cold volcanic mass flows at Augustine Volcano, Alaska: Natural Hazards and Earth System Science, v. 6, no. 5, p. 671–685.

Weaver, C.S., Grant, W.C., Malone, S.D., and Endo, E.T., 1981, Post-May 18 seismicity—Volcanic and tectonic implications, *in* Lipman, P.W., and Mullineaux, D.R., eds., The 1980 Eruptions of Mount St. Helens, Washington: U.S. Geological Survey Professional Paper 1250, p. 109–121.

Webley, P.W., Dean, K.G., Dehn, J., Bailey, J.E., and Peterson, R., 2010, Volcanic-ash dispersion modeling of the 2006 eruption of Augustine Volcano using the Puff model, *in* Power, J.A., Coombs, M.L., and Freymueller, J.T., eds., The 2006 eruption of Augustine Volcano, Alaska: U.S. Geological Survey Professional Paper 1769 (this volume).

Wessels, R.L., Coombs, M.L., Schneider, D.J., Dehn, J., and Ramsey, M.S., 2010, High-resolution satellite and airborne thermal infrared imaging of the 2006 eruption of Augustine Volcano, *in* Power, J.A., Coombs, M.L., and Freymueller, J.T., eds., The 2006 eruption of Augustine Volcano, Alaska: U.S. Geological Survey Professional Paper 1769 (this volume).

Woods, A.W., and Kienle, J., 1994, The dynamics and thermodynamics of volcanic clouds—Theory and observations from the April 15 and April 21, 1990, eruptions of Redoubt volcano, Alaska: Journal of Volcanology and Geothermal Research, v. 62, no. 1–4, p. 273–299.